remote sensing

MDPI

Article

Modelling Permafrost Characteristics and Its Relationship with Environmental Constraints in the Gaize Area, Qinghai-Tibet Plateau, China

Yudan Wang [1], Hao Chen [1,*], Zhuotong Nan [2,3] and Zhihai Shang [1]

[1] School of Geographical Sciences, Lingnan Normal University, Zhanjiang 524048, China
[2] Key Laboratory of Ministry of Education on Virtual Geographic Environment, Nanjing Normal University, Nanjing 210023, China
[3] Jiangsu Center for Collaborative Innovation in Geographical Information Resource Development and Application, Nanjing 210023, China
* Correspondence: chenhao@lingnan.edu.cn

Abstract: The impact of environmental constraints on permafrost distribution and characteristics of the remote western Qinghai-Tibetan Plateau (QTP) were seldom reported. Using augmented Noah land surface model, this study aims to elaborate the permafrost characteristics and their relationship with key environmental constraints in the Gaize, a transitional area with mosaic distribution of permafrost and seasonally frozen ground in the western QTP. There were two soil parameter schemes, two thermal roughness schemes, and three vegetation parameter schemes with optimal minimum stomatal resistance established using MODIS NDVI, turbulent flux, and field survey data. Forcing data were extracted from the China Meteorological Forcing Dataset (CMFD) and downscaled to 5 km × 5 km resolution. Results show that the error of simulated mean annual ground temperatures (MAGT) were less than 1.0 °C for nine boreholes. The Kappa coefficiency between three types of permafrost and three types of vegetation is 0.654, which indicates the close relationship between the presence of certain vegetation types and the occurrence of certain permafrost types in the Gaize. Permafrost distribution and characteristics of the Gaize are jointly influenced by both altitude and vegetation. The relationship of permafrost with environmental constraints over the Gaize is significantly different from that of the West Kunlun, a western, predominantly permafrost-distributed area.

Keywords: Noah land surface model; permafrost characteristics; environmental constraint; vegetation

Citation: Wang, Y.; Chen, H.; Nan, Z.; Shang, Z. Modelling Permafrost Characteristics and Its Relationship with Environmental Constraints in the Gaize Area, Qinghai-Tibet Plateau, China. *Remote Sens.* **2022**, *14*, 5610. https://doi.org/10.3390/rs14215610

Academic Editors: Guojie Hu, Jie Chen and Wenxin Zhang

Received: 6 October 2022
Accepted: 1 November 2022
Published: 7 November 2022

1. Introduction

The Qinghai-Tibet Plateau (QTP) plays a fundamental role in the formation of Northern Hemisphere climate due to its huge area, high altitude, and significant thermodynamic effects [1,2]. Permafrost is the main substrate of the QTP, with an area exceeding 1 million km^2 [3]. Modelling the thermal state, distribution, and characteristics of permafrost will help to elaborate the land surface processes over the QTP. It can also provide reliable land surface parameters for the regional or global climate models [4,5].

Many conceptual, empirical, and process-based models have been applied in the simulation of permafrost at scales from kilometres to hundreds of kilometres [6]. The distribution and characteristics of permafrost at high altitudes are largely determined by altitude, latitude, and longitude zonation [7], and they are greatly influenced by local environmental constraints such as snow cover [8,9], vegetation [10], substrate [11], soil texture [12], soil moisture [13], and geothermal [14]. The parametrization schemes of meteorological and environmental constraints are essential for the accurate modelling of permafrost [15], especially in the fine-scale permafrost modelling, due to the significant spatial heterogeneity. It is also imperative to quantify the impact of environmental constraints on the occurrence and characteristics of permafrost.

Permafrost over the QTP is characterized by low southern fringe air temperature (1–2 °C lower than that of the high latitude area), thin snowpack and high spatial heterogeneity of ground ice content (GIC), active layer thickness (ALT), and permafrost thickness [16,17]. Vegetation in the region comprises the alpine steppe, alpine meadow, and swamp meadow [18]. Owning to the scarcity of survey data, studies on the permafrost hydrothermal dynamics and its relationship with local environmental constraints are insufficient over the QTP. This is particularly true in the large transition zone between permafrost and seasonally frozen ground (SFG) [19]. Satellite, airborne, and field data show that the thermal, hydrological, climatic, and ecological processes of the mosaic permafrost areas are quite complex due to the changing permafrost dynamics [20–22]. Vegetation and gravel were reported to have marked influence over the hydrothermal regimes of the permafrost area of the QTP [23–25]. The relationship of permafrost and vegetation has been discussed in the Wudaoliang and the source area of the Datong River (SADR) in the eastern QTP [23,26]. It was found that vegetation tend to increase the evapotranspiration and decrease the absorbance of radiation of land surface in the permafrost areas of the QTP. However, few studies on this subject have been conducted in the arid western QTP. Moreover, employing simple empirical models and borehole data, those studies focused on the relationship of vegetation with the mean annual ground temperature (MAGT), whereas a land surface model (LSM), such as Noah, can simulate all the key permafrost metrics and quantify the relationship between environmental constraints and permafrost in spatial and temporal patterns [27]. A previous study has proven that an augmented Noah model works well in the simulation of permafrost distribution and characteristics of the whole QTP [28–30]. However, the simulation on the transitional area between permafrost and seasonal frozen ground was not satisfactory, due to the possible coarse resolution of 10 km × 10 km [19]. Moreover, augmentation to the Noah simulation on the permafrost area by Wu et al. [28], focuses on soil hydrothermal dynamics, with little consideration to the vegetation parameterization. Recent studies show that vegetation dynamics and stomatal resistance were sensitive parameters in Noah modelling on alpine grassland [31], and the default minimum stomatal resistance parameter used in Noah may not be suitable for alpine meadow areas of the QTP [32].

In this paper, Noah augmented by Wu et al. [28] was used to simulate the permafrost characteristics of Gaize, a transitional area with mosaic distribution of permafrost and seasonally frozen ground on the QTP. The Gaize area is covered by alpine steppe, alpine meadow, and sparse vegetation, thus the proper settings of vegetation parameters were discussed. Forcing data extracted from the China Meteorological Forcing Dataset (CMFD) [33] was downscaled to 5 km × 5 km by the Meteorological Distribution System for High-Resolution Terrestrial Modelling (MicroMet) [34] and verified at TGL station. Parametrization schemes, including soil, vegetation, and thermal roughness, were set up using MODIS NDVI, turbulent flux, and field survey data. The accuracy of the Noah simulation in the Gaize area was validated by nine pieces of borehole data and compared to another permafrost map based on field survey data. Finally, permafrost characteristics, as well as its relationship with environmental constraints in the Gaize area, were discussed.

2. Materials and Methods

2.1. Study Area and Data Source

The Gaize area (84.0°–86.0°E; 32.3°–34.0°N) (Figure 1a) is located on the southern fringe of the QTP with mosaic distribution of permafrost and SFG. The area is about 39.1×10^3 km^2, and the terrain is comparatively flat, with elevation ranges from 4400 m a.s.l. to 6000 m a.s.l. Mean annual air temperature (MAAT) at the Gaize weather station (4420 m a.s.l.) has been about 0 ºC during the past 30 years. The mean annual precipitation (MAP) is about 200 mm, and the average annual snow day is about 60 [35]. Vegetation in the Gaize area comprises alpine steppes, alpine typical meadows, and swamp meadows, with coverage ranging from 0 to 80% [36]. Soil in the Gaize area is rich in sand and gravel.

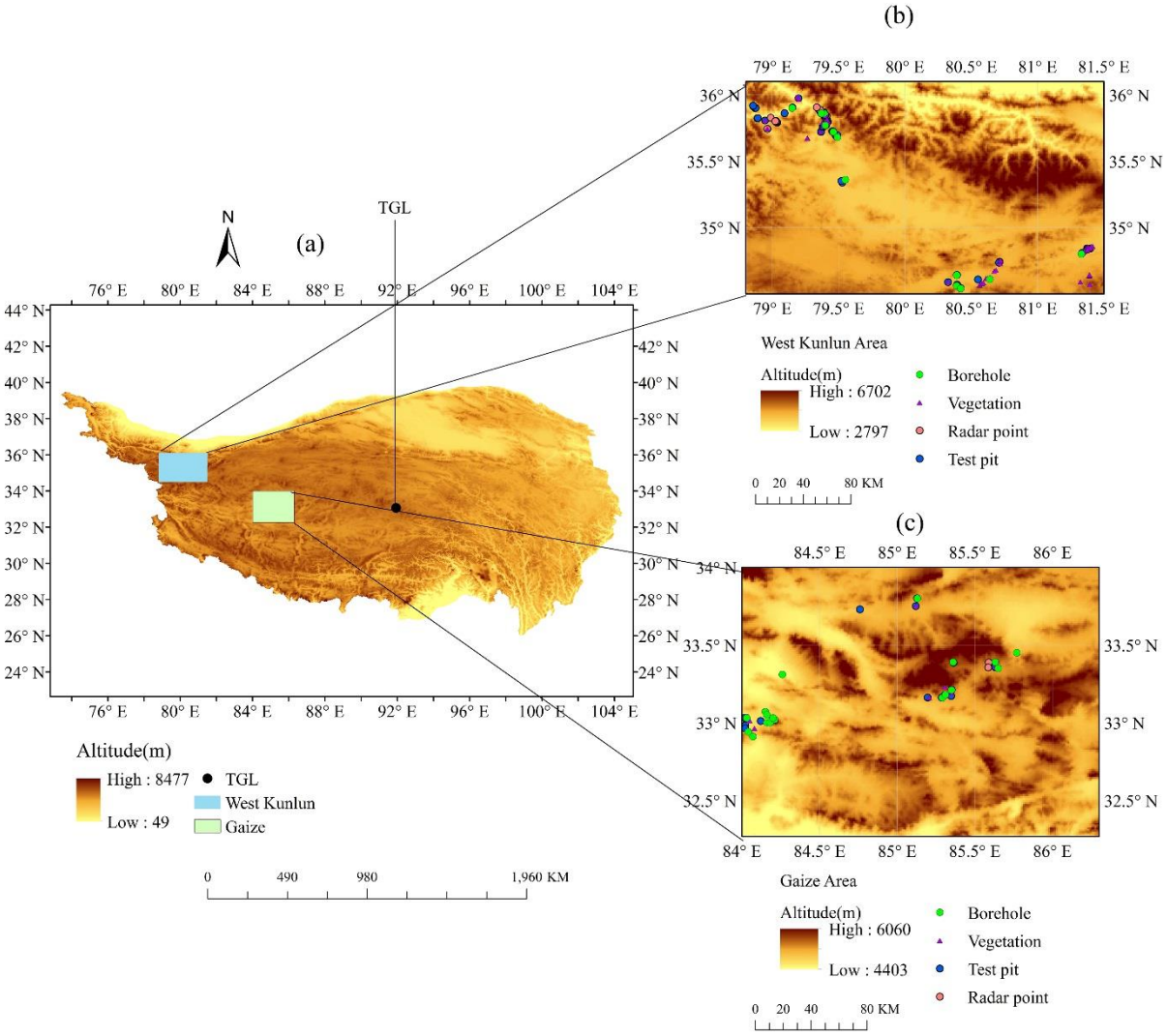

Figure 1. (**a**) Altitude of the QTP and locations of the TGL station, Gaize area, and West Kunlun area; (**b**) altitude and sampling sites of the Gaize area; (**c**) altitude and sampling sites of the West Kunlun area.

The West Kunlun area (78.8–81.5°E, 34.5–36.1°N) (Figure 1a) ranges in elevation from 2797 m a.s.l. to 6399 m a.s.l., with vast expanses of stable permafrost at western QTP. MAAT is −6.3 °C and MAP is around 50 mm. The area is sparsely covered with alpine steppes and desert steppes. Permafrost distribution and characteristics of the West Kunlun were simulated by the Noah model in previous work [37] and will be compared with that of the Gaize area.

Observation data from TGL station (Figure 1a), a typical permafrost monitoring site at 5100 m a.s.l. of the eastern QTP, were used to verify the forcing data used in this study. The TGL station lies on a gentle slope with alpine steppe coverage at central QTP. A 10 m high automatic weather station was installed in TGL, with measurements on meteorological factors, as well as soil moisture and temperature, at 5, 10, 20, and 40 cm depths.

Owning to the absence of data in the remote western QTP, a series of field surveys have been launched to obtain reliable data at permafrost areas of the QTP under harsh environment and various landscapes [38–41]. From 2009 to 2014, 22 boreholes (6–56 m deep) were drilled, 20 test pits were excavated, 14 ground penetrating radars traverses were obtained, and 34 vegetation quadrats were measured in the Gaize area (Figure 1b). Ground temperatures were measured by temperature probes, located in the boreholes, at 0.5 m over the first 3 m and every 1.0 m thereafter. Measurements were recorded once every year since

2010, and the MAGT at each borehole were found to be stable [35]. Similar monitoring works have also been done at the West Kunlun area and reported by Chen et al. [37] (Figure 1c). The observed meteorological data and borehole data used in model validation were downloaded from National Tibetan Plateau Data Center (https://data.tpdc.ac.cn/, accessed on 3 March 2021) and extracted from "a synthesis dataset of permafrost for the Qinghai-Xizang (Tibet) Plateau, China (2002–2018)" with reference to data records of previous works [35,42]. The DEM data at 1 km × 1 km resolution were provided by the International Scientific Data Service Platform (http://datamirror.csdb.cn, accessed on 10 August 2021).

2.2. Augmented Noah LSM

The original Noah LSM 3.4.1 model was augmented to meet the challenges of hydrothermal simulation on the permafrost areas of the QTP. Main augmentations consist of soil stratification, simulation depth at about 15 m, combinations of two thermal roughness schemes that are suitable for sparse or well-vegetated ground, respectively, a new soil thermal conductivity scheme account for gravelly soil, and a new hydraulic conductivity scheme account for ground ice. Details of the augmented schemes for thermal roughness, soil thermal conductivity, and soil hydraulic conductivity in Noah can be found in Wu et al. [28], and source code can be downloaded here (https://doi.org/10.17605/OSF.IO/G7JQR, accessed on 22 August 2021). Performance of the augmented Noah in simulating soil hydrothermal dynamics, from ground surface to 15m deep, were validated against observations of TGL station (Figure 1a), a permafrost site at the central QTP [28], and proved to be successful in previous studies [29,30].

2.3. Forcing Data Downscaled by MicroMet

Forcing data of the Noah model include air temperature, air pressure, wind speed, wind direction, downward shortwave radiation (DSR), downward longwave radiation (DLR), relative humidity, and precipitation. In this study, they were extracted from the CMFD at 0.1° × 0.1° (approximately 10 km × 10 km) resolution and downscaled into 5 km × 5 km by the MicroMet. The CMFD was a meteorological dataset produced by merging multi-source data, including precipitation data derived from remote sensing, a reanalysis meteorological dataset, and in-situ observation data. Accuracy of the CMFD was validated in many permafrost and watershed hydrology simulations conducted on the QTP [28,29,42]. CMFD is provided by National Cryosphere Desert Data Center (http://www.ncdc.ac.cn, accessed on 10 May 2020).

MicroMet aims to provide high-resolution meteorological forcing data to spatially distributed terrestrial models [34]. It is an integrated module of Snowmodel, and it has been widely applied in meteorological data preparation, scaling, and interpolation for terrestrial models over cold regions [43–46]. In the MicroMet downscaling process, meteorological grids are spatially interpolated into the target resolution using a Barnes objective analysis scheme, which adopts a Gaussian distance-dependent weighting function [47]. Then, the interpolated grids are adjusted according to quasi-physical models of the eight meteorological factors. For example, the interpolated precipitation and air temperature grids are adjusted according to their respective lapse rate based on elevation. Relative humidity is adjusted by the relatively linear relationship between dew-point temperature and elevation. Wind speed and direction are adjusted using a model based on their relationship with topographic slope and curvature [48]. DSR is calculated at the model time with consideration of the influence by cloud cover, direct and diffuse solar radiation, as well as topographic slope and aspect. DLR is calculated while taking into account cloud cover and elevation-related variations following Iziomon et al. [49]. Details of the above adjustment models can be referred to in Liston et al. [34].

2.4. Validation of Forcing Data

We further validated the MicroMet downscaled CMFD forcing data (5 km × 5 km) at an alpine steep vegetated permafrost site named TGL (Figure 1a). Meteorological forcing data at the location of the TGL were extracted from the downscaled CMFD data, from 1 April 2007 to 31 December 2010, and compared with observation data of the TGL. Chen et al. reported the strong correlation between CMFD forcing data and TGL observation data regarding daily air temperature and monthly precipitation with Pearson correlation analysis. After the MicroMet downscaling, the correlation between downscaled CMFD data and the TGL observation data is still strong for the daily air temperature ($r = 0.98$, $p < 0.01$) (Figure 2a) and the monthly precipitation data ($r = 0.94$, $p < 0.01$) (Figure 2b). Augmented Noah modelling on the hydrothermal processes of the TGL station were done with the downscaled CMFD data and the TGL observation data, respectively. Results show that the Nash–Sutcliffe model efficiency coefficients (NSE) for ground soil temperature (0.05 m) simulation using both data are above 0.9 (Figure 2c,d). Wu et al. has validated that the augmented Noah can successfully simulate the soil temperature and soil moisture of TGL station, from 0 to 15 m, with observed meteorological data. Figure 2c,d proved that the downscaled CMFD data are suitable in simulating the hydrothermal processes of permafrost areas on the QTP with similar accuracy to the observation data.

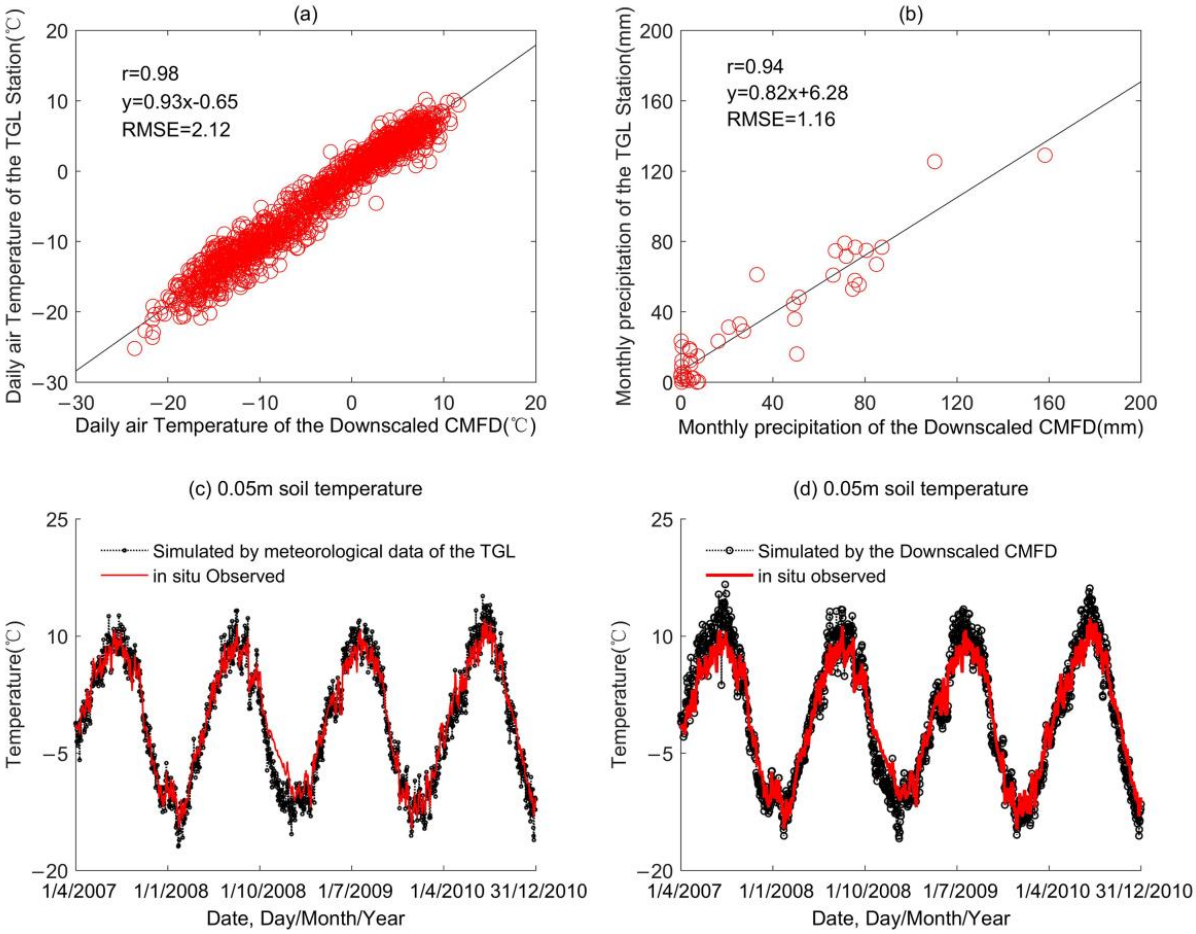

Figure 2. Plots of (**a**) the 2 m daily air temperature; (**b**) the monthly precipitation extracted from downscaled China Meteorological Forcing Dataset (CMFD) against observations of TGL station from 1 April 2007 to 31 December 2010; The observed 0.05 m soil temperature contrast to the 0.05 m soil temperature simulated using (**c**) observed meteorological data of TGL station and (**d**) downscaled CMFD data at extracted at TGL station.

2.5. Modelling the Permafrost Characteristics of the Gaize

As the MAGTs of the validation boreholes were stable since 2010, the year 2010 was used as the reference year. Forcing data from 2001 to 2010 were extracted from the downscaled CMFD at 30 min steps. The model was spun up for 10 years to avoid possible influence brought by the initial conditions. Key permafrost metrics, including MAGT, ALT, and GIC of the Gaize area, were simulated by the augmented Noah at 5 km × 5 km resolution, with combined soil, thermal roughness, vegetation parameter schemes, and deep soil temperature parameter, according to the ground conditions of the specific grid. The simulation depth was 15.82 m, which is deeper than the lower limits of the depth of zero annual amplitude (DZAA) of the Gaize. The simulated permafrost metrics of Gaize were validated against nine representative pieces of borehole data selected from the 22 boreholes drilled by the investigation projects conducted from 2009 to 2014 [41]. The criteria for representative boreholes are their consistency with the predominant land cover, soil texture, and altitude of its grid. Details of the 22 drilled boreholes can be referred to in Chen et al. [35]. Table 1 shows the details of the nine representative boreholes. Simulated ALT and GIC were calculated according to the variation of ground temperature and soil moisture [37]. A permafrost distribution map of the Gaize was compiled according to the simulated MAGT.

Table 1. Details of nine representative boreholes in the Gaize area.

ID	Code	Latitude (°)	Longitude (°)	Altitude (m)	Underlying Surface
1	ZK01	32.94	84.04	4730	Barren of sparsely vegetated (BSV)
2	ZK02	32.91	84.07	4840	Alpine steppe
3	ZK10	33.03	84.20	4890	BSV
4	ZK12	33.16	85.29	5028	BSV
5	ZK14	33.21	85.35	5196	Alpine steppe
6	ZK22	33.39	85.63	5095	Alpine steppe
7	ZK18	33.39	85.36	5105	BSV
8	ZK21	33.80	85.13	5018	Alpine steppe
9	ZK17	33.39	85.63	5104	Alpine meadow

2.5.1. Soil Parameter Scheme

Soil was vertically stratified into 23 layers, and layer soil parameters were set according to the layer soil type to embody soil heterogeneity. Borehole observations show that the Gaize area is characterized by varied content of gravelly soil from surface to bedrock. Previous studies indicated that the augmented Noah, with default parameter sets of soil types, was applicable in the regional simulation on the QTP [28,50]. In this study, two soil parameter schemes, namely the ZK14 scheme and ZK01 scheme, were developed according to the soil profile of the representative boreholes. The ZK01 scheme is based on the soil profile of borehole ZK01, where general gravel content is over 30%, the ZK14 scheme is based on borehole ZK14, where gravelly soil is less than 30%, and remaining contents are sand and loam. The augmented Noah adopts different soil thermal schemes for gravelly and non-gravelly soil. Thus, distribution of the two schemes was determined by the general content of gravelly soil in the simulated grid. The gravel content of soil profiles in the Gaize area was extracted from the China soil properties dataset [51] and verified by the borehole data. Details of the two soil parameter schemes can be found in Table 2, and the distribution of the two schemes can be found in Figure 3.

Table 2. Landscape and soil profiles of the two soil parameter schemes of the Gaize area.

Scheme	Landform and Landscape	Surface Layer	Subsurface Layer1	Subsurface Layer2	Subsurface Layer3	Bottom Layer
ZK14	Plain, Carex and Kobresia	sandy loam,	loamy Sand	sand	gravelly soil	bedrock,
ZK01	Plain, Stipa capillata Linn	loamy Sand	sand	gravelly soil	gravelly soil	bedrock

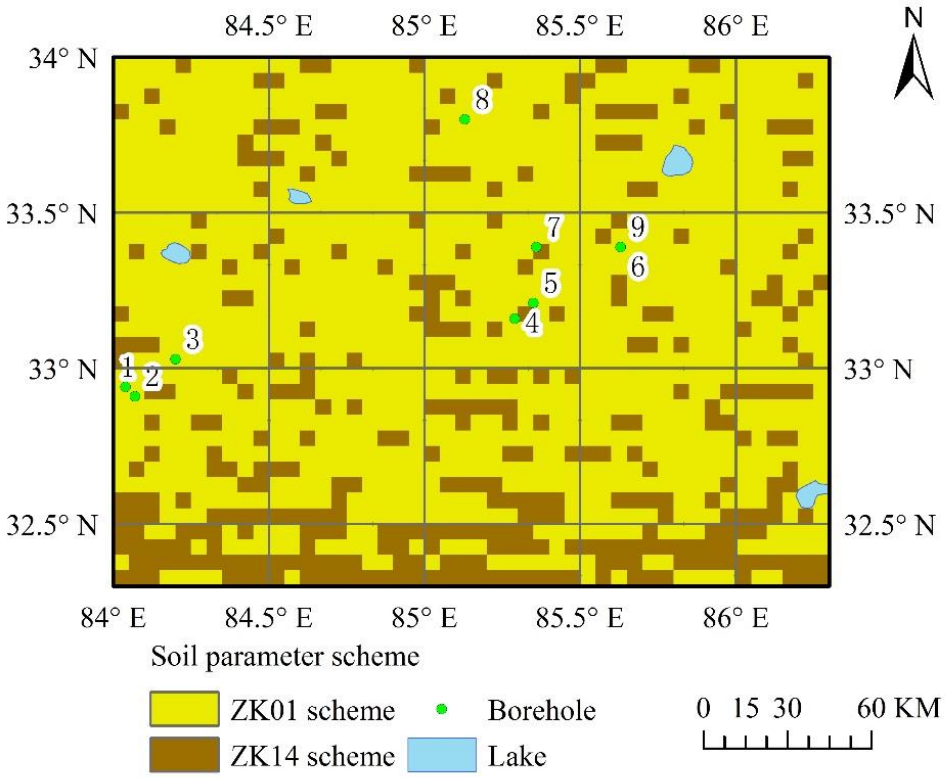

Figure 3. Distribution of soil parameter schemes in the Gaize area (Borehole number 1 to 9 correspond to the borehole ID in Table 1).

Soil depth for surface layer, subsurface layer1, subsurface layer2, subsurface layer3, and bedrock are 0−0.12 m, 0.12−1.88 m, 1.88−3.02 m, 3.02−6.82 m, and 6.82−15.82 m, respectively.

2.5.2. Thermal Roughness Parameter Scheme

Depending on vegetation coverage, the augmented Noah provides two thermal roughness schemes, namely Z95 and Y08, for simulations on alpine meadow and sparsely vegetated ground, respectively. In this study, vegetation coverage over the Gaize was estimated using the dimidiate pixel model (DPM), which assigns the total NDVI value, in a pixel of an image, as the linear sum of weighted NDVI values from bare soil and green vegetation. DPM was proven to be the most popular approach to estimating vegetation coverage, at resolutions ranging from metres to kilometres, in the past three decades [52]. The vegetation coverage of a mixed pixel is calculated by Equation (1) in the DPM:

$$f_c = (NDVI_p - NDVI_{soil})/(NDVI_\infty - NDVI_{soil}) \quad (1)$$

where f_c stands for the vegetation coverage. $NDVI_p$ stands for the NDVI of the mixed pixel for vegetation and soil. $NDVI_{soil}$ represent the NDVI for the pure barren land. $NDVI_\infty$ stands for the NDVI for the pure vegetation.

Growing seasons of the vegetation in the Gaize last from April to September [53]. Hence, average maximum MODIS NDVI (MOD13Q1) from April to September, during 2000 to 2010, were extracted as $NDVI_p$ for each grid in the Gaize. Many studies use constant $NDVI_\infty$ and $NDVI_{soil}$ for specific vegetation types in the DPM [54,55]. However, the suggested groups of $NDVI_\infty$ and $NDVI_{soil}$ for grasslands, in previous studies, may not be appropriate for alpine grasslands on the QTP. In this study, the corresponding NDVI values of the 0.5% and 99.5% cumulative percentages for NDVI over the Gaize area, from 2000 to 2010, are regarded as the $NDVI_{soil}$ (0.5%) and $NDVI_\infty$ (99.5%) values to avoid the possible bias in the NDVI product [56]. Distribution of vegetation coverage of the Gaize was calculated in Equation (1) and rectified with field observations (Figure 4a).

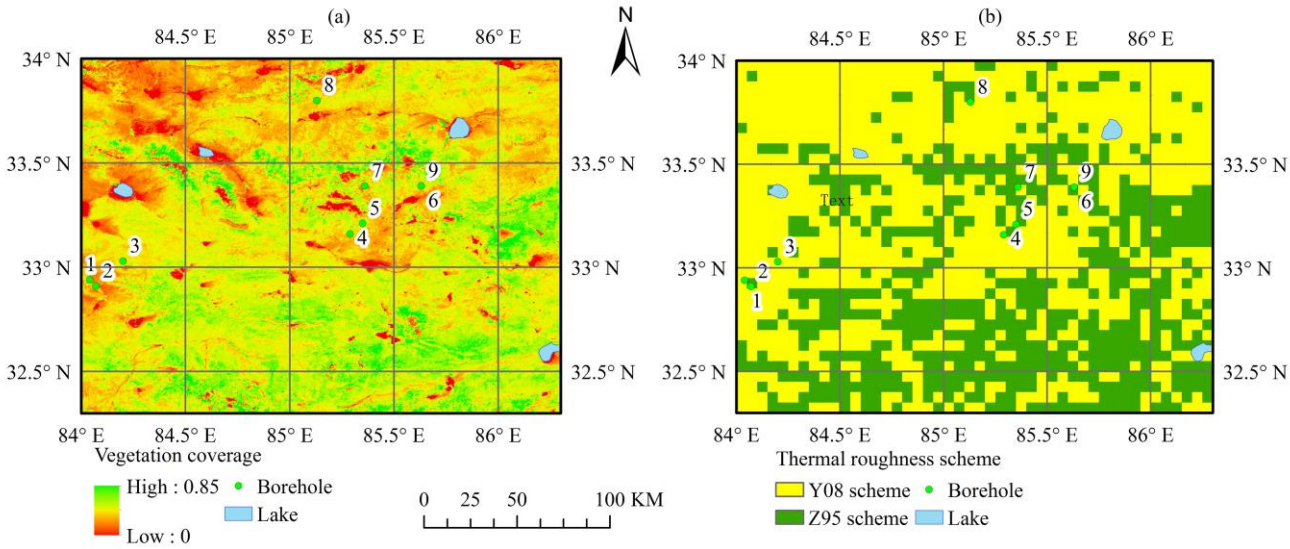

Figure 4. Distribution of (**a**) vegetation coverage and (**b**) thermal roughness scheme in the Gaize area (Borehole number 1 to 9 correspond to the borehole ID in Table 1).

Taking 0.30 as the threshold of vegetation coverage, a distribution map of barren land or sparsely vegetated (BSV) and alpine grassland was generated and upscaled to 5 km × 5 km by the ArcGIS resampling tool. Replacing the BSV with the Y08 scheme [57] and the alpine grassland with the Z95 scheme [58], a thermal roughness scheme distribution map can be seen as Figure 4b.

2.5.3. Vegetation Parameter Scheme

BSV, alpine steppe, and alpine meadow are the three main types of vegetation over the Gaize area [36]. BSV and alpine grassland can be separated by a 0.3 threshold of vegetation coverage. However, it is hard to distinguish alpine steppe and alpine meadow only by vegetation coverage. We introduced an updated distribution map, about diverse vegetation types over the QTP, by Wang et al. [59]. Validated by field survey data, the map was compiled using the decision tree classifier method and multi-source data, including field vegetation samples, MODIS land surface temperature (LST), elevation, and enhanced vegetation index (EVI). The original 1 km × 1 km map was upscaled to 5 km × 5 km using the ArcGIS resample tool, and the vegetation over the Gaize area was reclassified into BSV, alpine steppe, and alpine meadow. Figure 5 shows the distribution of the three vegetation parameter schemes of BSV, alpine steppe, and alpine meadow.

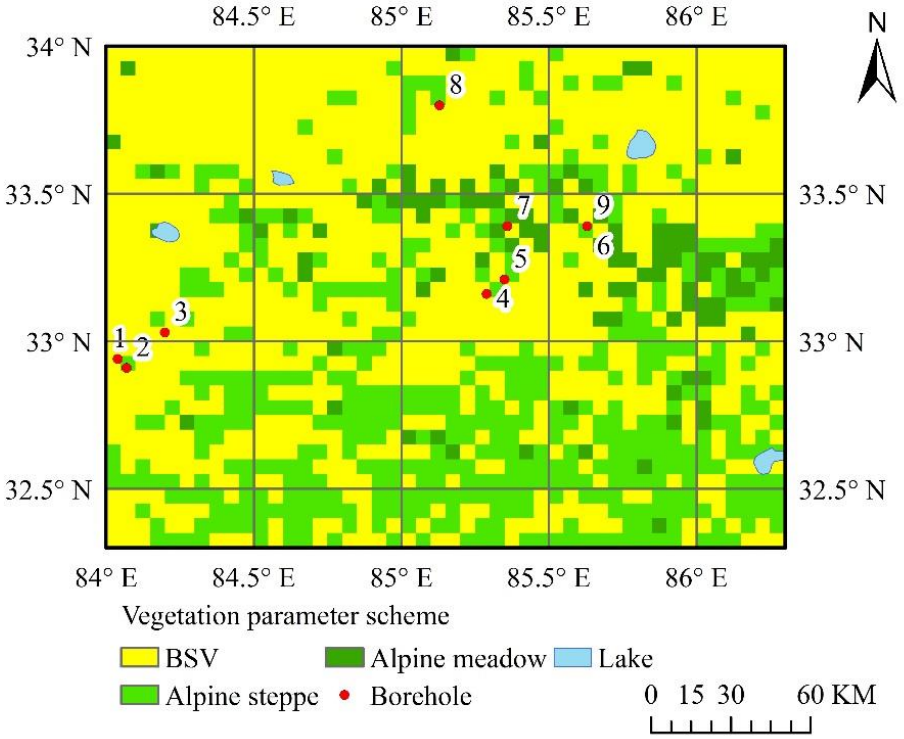

Figure 5. Distribution of vegetation parameter schemes in the Gaize area (Borehole number 1 to 9 correspond to the borehole ID in Table 1).

2.5.4. Deep Soil Temperature (DST) Setting

Minimum canopy stomatal resistance(r_{cmin}) and vegetation coverage were proved to be sensitive vegetation parameters in Noah modelling [31]. However, the default vegetation parameters may not be appropriate in alpine grassland. Based on field turbulent flux data, Chang et al. [32] suggested that the optimal r_{cmin} for alpine grassland of the northeastern QTP is 19, rather than the default 40 applied to the vegetation type of 'grassland' in the Noah parameter table [60]. In this study, the BSV scheme has adopted the default parameters of 'Barren or Sparsely Vegetated' type, and the alpine steppe and alpine meadow schemes have adopted the default parameters of the 'grassland' type in the Noah parameter table of vegetation. Then, the default vegetation coverage parameters of the alpine steppe scheme and the alpine meadow scheme were replaced by the values calculated by Equation (1), and r_{cmin} = 19 was adopted for the alpine steppe and the alpine meadow schemes.

The deep soil temperature (DST) parameter is used as a lower boundary in the Noah model, and it is generally set as the soil temperature at 40 m [30,37]. Boreholes ZK21 and ZK22 in Gaize are deeper than 40 m, and the DSTs are recorded accordingly. The remaining boreholes are around 15 m deep, and the DSTs are calculated according to the geothermal gradient at 15 m depth. As 15 m depth has generally reached the bedrock area and the depth is deeper than the DAZZs in the Gaize, accuracy of the method is acceptable. Field data show that the alpine meadow area tends to have a much lower soil temperature than that of alpine steppe and sparse vegetation at the same altitude. Borehole ZK17 is the only one on the alpine meadow area, so its DST were used as the DSTs of all the grids covered with alpine meadow. The remaining eight borehole DSTs were linearly fitted, with their altitude, into a regression equation (Equation (2)). The regression curve can be seen in Figure 6. Grid cells covered with alpine steppe and sparse vegetation adopt Equation (2) to calculate the DST.

$$y = -0.006645x + 34.14 \quad (2)$$

where y is DST (°C) and x is altitude (m); the linear correlation coefficient r = −0.91 ($p < 0.01$); the determination coefficient of the regression model R2 = 0.83.

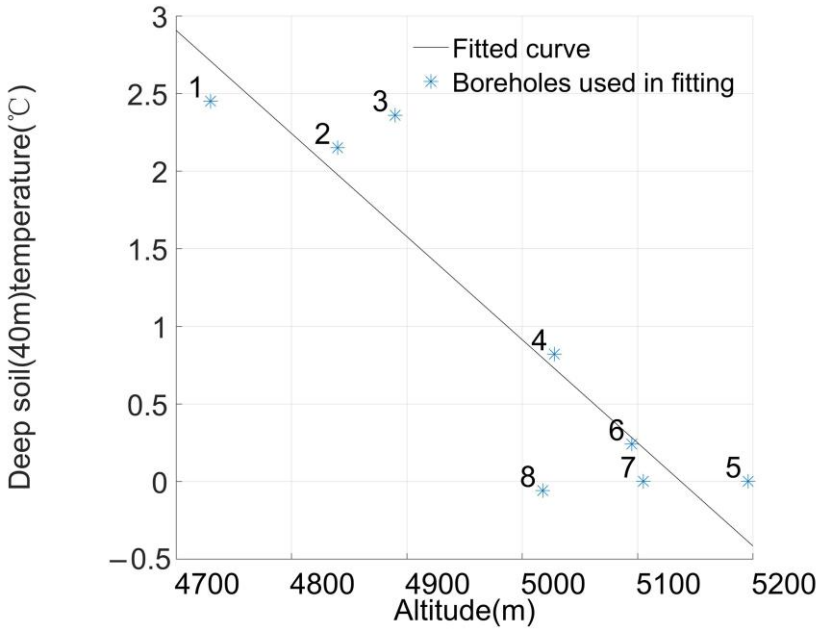

Figure 6. Linear regression curve of Deep soil temperature (DST) (40 m) and altitude in the Gaize area.

3. Results

3.1. Borehole Validation

Table 3 shows that the simulation errors of the MAGTs at the DZAA of all nine boreholes are within 1 °C. The correlation coefficient between the simulated and the observed MAGT is 0.93, and RMSE is 3.51 (Figure 7). There were four of the representative boreholes that were overestimates, and the other five were underestimates, which indicated that the simulation accuracy was acceptable, and the biases were randomly distributed. However, the simulated MAGTs of borehole ZK21 were above 0 °C, whereas the observed ones were below 0 °C. Thus, the grid cells containing borehole ZK21 will be judged as SFG according to the simulated MAGT, but they will be judged as permafrost according to the observed MAGT. This mismatch leads to the main discrepancy in permafrost judgements over the unstable permafrost area of the Gaize. Chen et al. [35] suggested that the MAGT of borehole ZK22 ought to be lower than the observed −0.1 °C, considering the situation of neighbouring boreholes. Errors of observation may come from the disturbed soil during the observation period. This discrepancy suggests that higher accuracy is both required for field survey and model simulation in the transitional and MAGT-sensitive permafrost areas of the Gaize. Optimal vegetation and soil parameters that match the ground conditions of the Gaize are needed in modelling. Bias transmitted from scale matching, borehole data recording, and parameter setting also cannot be neglected.

Table 3. Simulated and observed mean annual ground temperature (MAGT) of the nine representative boreholes in the Gaize area.

ID	Code	Simulated MAGT (°C)	Observed MAGT (°C)	aError (°C)
1	ZK01	2.3	2.1	0.2
2	ZK02	1.5	2.0	−0.5
3	ZK10	1.8	2.0	−0.2
4	ZK12	0.7	0.8	−0.1
5	ZK14	−0.1	−0.4	0.3
6	ZK22	−0.4	−0.1	−0.3
7	ZK18	−0.1	−0.5	0.4
8	ZK21	0.4	−0.4	0.8
9	ZK17	−2.4	−1.9	−0.5

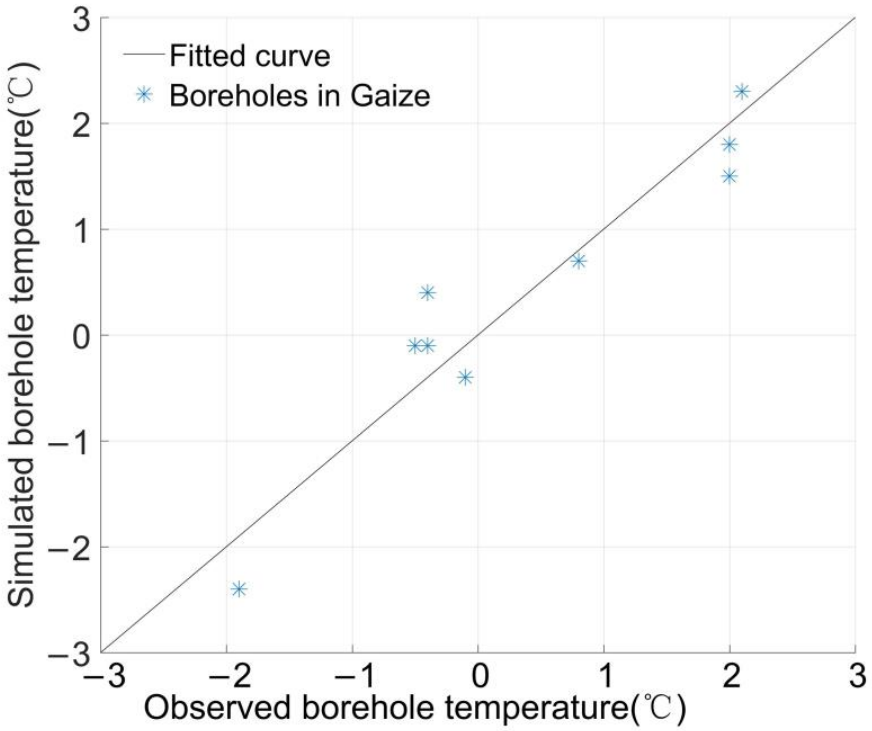

Figure 7. Plots of simulated and observed MAGT of nine boreholes in the Gaize area.

3.2. MAGT, ALT and GIC Distribution

The simulated distribution of MAGT, ALT, GIC, altitude, vegetation, and MAP can be seen in Figure 8.

Pearson correlation analysis between key permafrost metrics (MAGT, ALT, and GIC) and important environmental constraints (altitude, vegetation, and MAP) can be seen in Table 4.

Table 4. Correlation coefficient matrix of environmental constraints with key permafrost metrics in the Gaize area.

Metrics	MAGT	GIC	ALT
Altitude	−0.669	0.341	−0.295
MAP	0.018	0.056	−0.057
Vegetation coverage	−0.458	0.354	−0.344
MAGT	-	−0.523	0.773
ALT	0.773	0.280	-

Table 4 shows that the MAGT (Figure 8a) has a strong negative correlation with the altitude (Figure 8b) ($r = -0.669$, $p < 0.01$), moderate negative correlation with the vegetation coverage (Figure 8f) ($r = -0.458$, $p < 0.01$), and no significant correlation with annual precipitation (Figure 8e) ($r = 0.018$, $p > 0.05$), which suggests that permafrost distribution in the Gaize is constricted by altitude and vegetation. The MAGT correlation with altitude in the Gaize is weaker than the predominantly permafrost-distributed West Kunlun area ($r = -0.863$, $p < 0.01$) [37], which indicates that the local environmental factors have a higher impact on the MAGT in the Gaize.

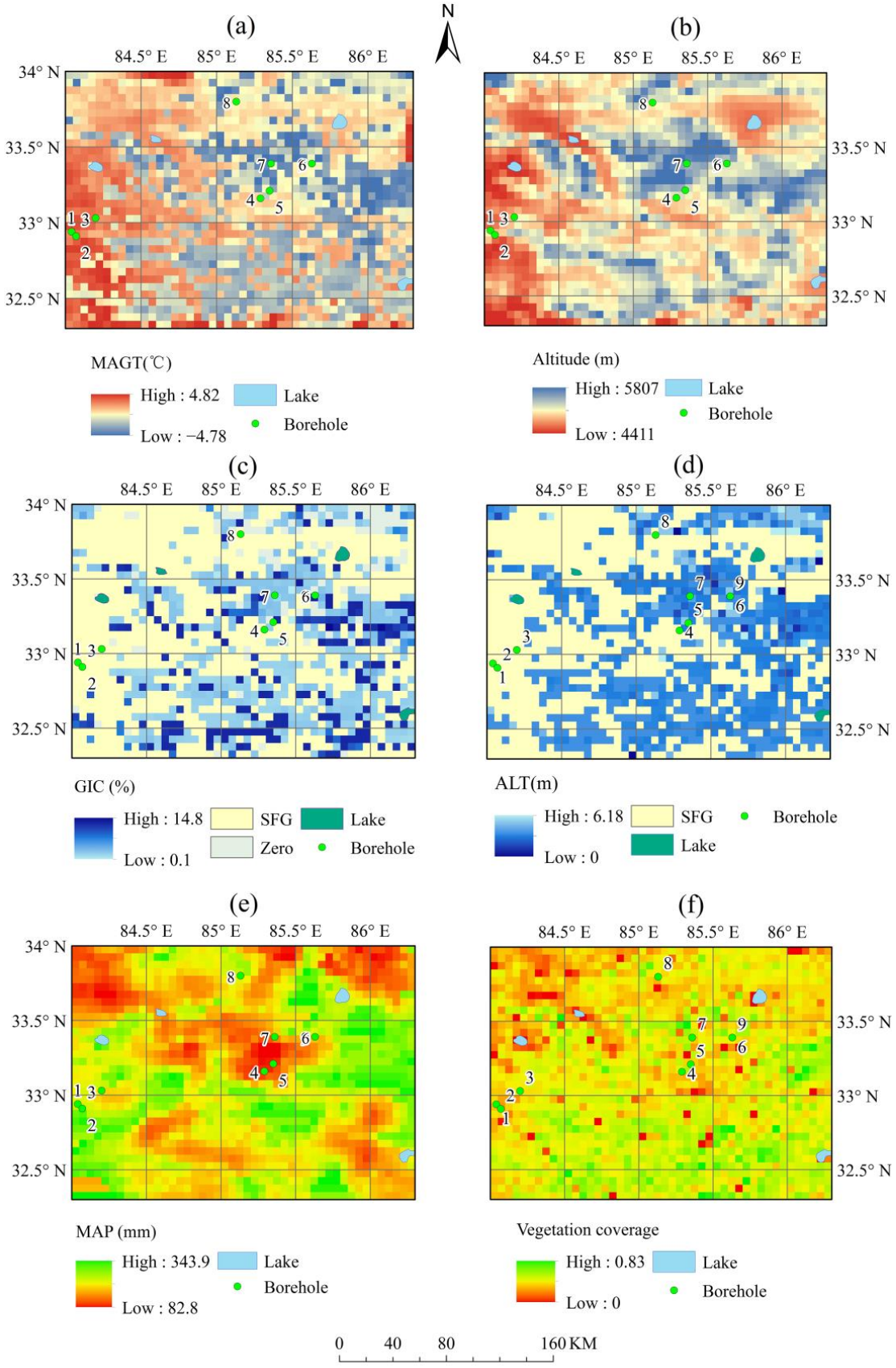

Figure 8. Distribution of (**a**) simulated MAGT; (**b**) altitude; (**c**) simulated ground ice content (GIC); (**d**) simulated Active layer thickness (ALT); (**f**) Mean annual precipitation (MAP); (**e**) vegetation coverage in the Gaize area (Borehole number 1 to 9 correspond to the borehole ID in Table 1).

The GIC (Figure 8c) is negatively correlated with the MAGT distribution (r = −0.523, $p < 0.01$) and the ALT (r = −0.280, $p < 0.01$), and it is positively correlated with the altitude (r = 0.341, $p < 0.01$) and the vegetation coverage (r = 0.354, $p < 0.01$). The simulated highest grid ice content (14.8%) of the Gaize is lower than that of the West Kunlun (21.4%) [37]. Areas with high ice content mainly distribute around glaciers or in the lacustrine deposits area of the West Kunlun, while they distribute in areas with high vegetation coverage in the Gaize. In contrast, MAP has no significant correlation with GIC. It is evident that altitude, vegetation coverage, and landform have greater impacts on the magnitude and distribution of ice content in the two areas than precipitation does. The ALT (Figure 8d) shows a strong positive correlation with the MAGT (r = 0.773, $p < 0.01$), a weak negative correlations with altitude (r = −0.295, $p < 0.01$) and vegetation coverage (r = 0.344, $p < 0.01$), and no significant correlations with MAP (r = −0.057, $p > 0.05$). Among all the variants, MAGT has the strongest correlation with ALT and GIC. Higher MAGT means higher ALT and less GIC in the Gaize area. Correlation coefficients of the vegetation coverage are similar to that of the altitude in their Pearson correlation analysis with the three permafrost metrics in the Gaize, which indicate that vegetation may have similar controlling strength as altitude on the permafrost characteristic of the Gaize.

3.3. Permafrost and ALT Classification

Permafrost can be classified as extremely stable, stable, sub-stable, transitional, unstable, and extremely unstable according to the MAGT range [7]. Figure 9a and Table 5 show the distribution of permafrost and SFG in the Gaize area. The average altitude and average MAGT of the Gaize is near to that of the unstable permafrost. The grid cells of the SFG of the Gaize accounts for 54.3% of the total cells, which is slightly higher than that of the permafrost. The altitudinal distribution of stable permafrost, sub-stable permafrost, transitional permafrost, unstable permafrost, and SFG severely overlap (Table 5), which means the altitudinal zonality of permafrost and SFG in the Gaize is not remarkable. Figure 9b shows that ALTs in the Gaize are mainly between 0 and 4 m, which accounts for 39.8% of the total grid cells and 87.1% of the permafrost grid cells.

Table 5. MAGT, altitude, and total grid cell counts of each permafrost type in the Gaize area.

Permafrost Type	MAGT (°C)	Average MAGT (°C)	Altitude (m)	Average Altitude (m)	Total Grid Cells	Percentage (%)
Extreme stable permafrost	<−5.0	–	–	–	–	–
Stable permafrost	−3.0–−5.0	−3.6	5618–4950	5324	125	8.0
Sub-stable permafrost	−1.5–−3.0	−2.2	5807–4783	5116	285	18.2
Transitional permafrost	−0.5–−1.5	−1.0	5790-4703	5091	178	11.4
Unstable permafrost	0–−0.5	−0.3	5643–4500	5037	127	8.1
Seasonally frozen ground (SFG)	>0	1.5	5498–4411	4879	849	54.3
Gaize area	−4.8–4.8	0.0	5807–4411	4995	1564	100.0

3.4. Permafrost Distribution Map

A 250 m × 250 m permafrost map (ALP map) (Figure 10a) was produced using the altitudinal limit of permafrost (ALP) model, which determines the lower boundary of permafrost under alpine steppe, through borehole data, at four slope aspects: 4950 m a.s.l. at the north, 5100 m a.s.l. at the south, as well as 5000 m a.s.l. in the east and in the west [35]. The permafrost map has been widely used as ground truth for assessment in many studies [28,61,62]. The ALP map of the Gaize (Figure 10a) was upscaled to the resolution of 1 km × 1 km (Figure 10b). A 5 km × 5 km permafrost distribution map (MAGT map) of the Gaize (Figure 10c) is produced using the augmented Noah-simulated MAGT. Then, 0 °C was taken as the threshold to distinguish permafrost and SFG in the MAGT map. Then, it is downscaled to 1 km × 1 km (Figure 10d) resolution to make a comparison with the ALP map. Results show that the MAGT map of the Gaize contains 17.9 × 103 km^2 permafrost, accounting for 45.7% of the total area, while SFG is 21.0 × 103 km^2, accounting for 53.8% (Figure 2d). In contrast, the ALP map of the Gaize contains 18.9 × 103 km^2 of

permafrost, accounting for 48.3% of the total area, while SFG is 20.0 × 103 km^2, accounting for 51.2% (Figure 2b). The Kappa coefficient for Figure 3b,d is 0.48, indicating that the two maps moderately agree with each other. The discrepancy of permafrost distribution in the two maps is 2.6% and mainly lies in areas with mixed vegetation cover, where the altitudinal limit of permafrost may be influenced by the distribution of vegetation coverage.

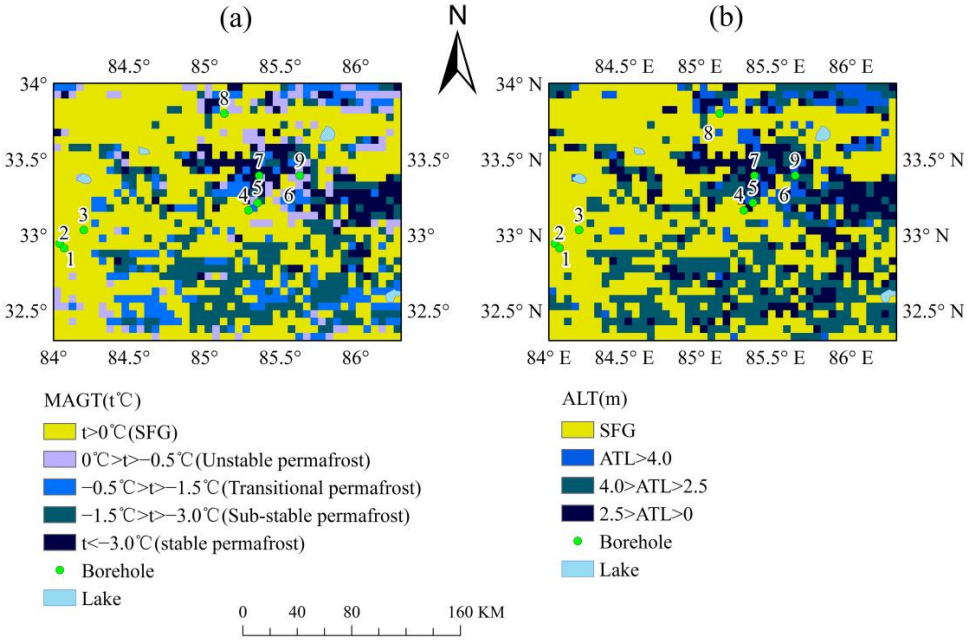

Figure 9. (**a**) Permafrost types based on the MAGT and their distribution in the Gaize area; (**b**) ALT distribution map of the Gaize area (Borehole number 1 to 9 correspond to the borehole ID in Table 1).

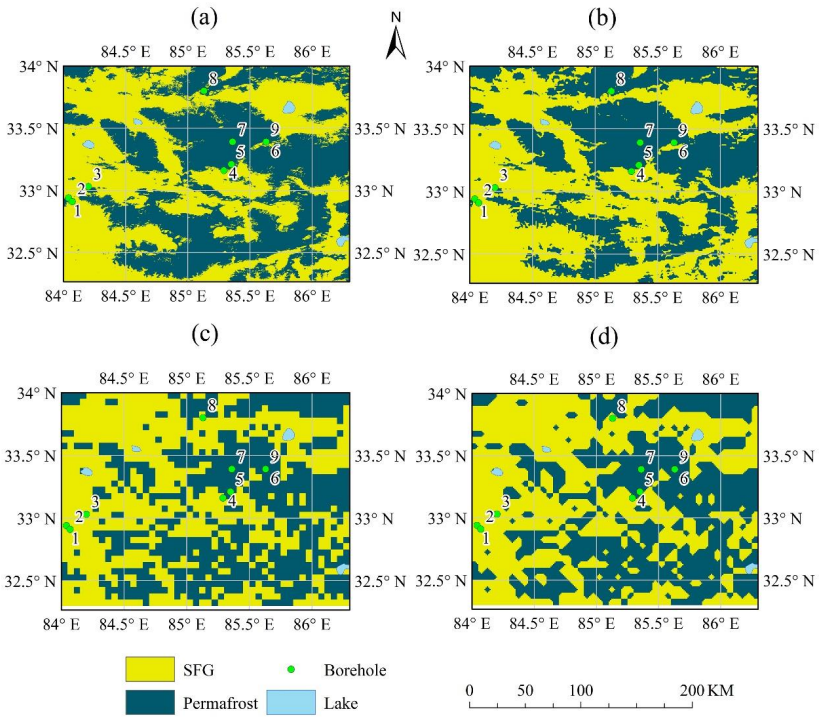

Figure 10. (**a**) Permafrost distribution map of the Gaize, based on the ALP model, with 250 m × 250 m resolution; (**b**) resampled permafrost distribution map of the Gaize, based on the ALP model, with 1 km × 1 km resolution; (**c**) permafrost distribution map of the Gaize, based on the MAGT model, with 5 km × 5 km resolution; (**d**) resampled permafrost distribution map of the Gaize, based on the MAGT model, with 1 km × 1 km resolution (Borehole number 1 to 9 correspond to the borehole ID in Table 1).

4. Discussion

4.1. Modelling Resolution and Parameter Schemes

Finer resolution in modelling can improve the simulation accuracy and the representativeness of borehole data. However, mapping resolution finer than 5 km in permafrost areas will face the challenge of a complex hydrothermal process such as lateral heat flow. Thus, 5 km resolution was adopted in the Noah simulation of this study.

Soil and vegetation are two crucial environmental constraints on permafrost distribution in the arid western QTP. The spatial heterogeneity of soil and vegetation can be presented by soil and vegetation parameter schemes in Noah. Table 6 shows the meteorological and environmental conditions of the Gaize and the West Kunlun area [37]. The Gaize locates southerly to the West Kunlun with higher MAAT and MAP. Thus the variation in vegetation species and coverage are higher in the Gaize. In contrast, West Kunlun is sparsely vegetated with remarkable soil heterogeneity due to the large altitude range and widely spread glaciers, river valley, and lacustrine deposits. Liu et al. [63] reported that distribution of soil texture, for soil layers between 0–3 m, was mainly affected by MAAT, MAP, and NDVI in the QTP. As the magnitude of MAP and NDVI are low, and MAAT was closely related with altitude in the West Kunlun, altitudinal zonality of permafrost was more remarkable in the West Kunlun than in the Gaize. Vegetation in the Gaize area has significantly disturbed the altitudinal zonality of permafrost. Thus, proper setting of the vegetation parameter scheme will help to improve the accuracy of permafrost simulation in the Gaize. However, the reduction in uncertainty in permafrost simulation over the Gaize area has always been challenging [3]. Boreholes were insufficiently and unevenly drilled in the Gaize during the past field surveys. Daily records of ground temperature and soil moisture are still absent, which limits the available validation of the Noah simulation. Although the augmented Noah has been validated to be applicable in hydrothermal simulation over the permafrost area of the QTP in many papers, its ability to simulate the impact of vegetation over permafrost at a finer resolution still needs further investigation. Moreover, many pieces of borehole data were abandoned given that the altitude, vegetation cover, or soil texture of the borehole site were not in accordance with the average conditions of the grid they locate. Thus, further investigation that aims to collect more reliable data at proper sites with typical vegetation types are needed, in which remote sensing products can help to determine the consistency of borehole data with the grid cell they locate.

Table 6. Environmental and meteorological factors at the West Kunlun and the Gaize area.

Areas	Mean Annual Air Temperature (MAAT) (°C)	MAP (mm)	Latitude (°)	Elevation (m)	Vegetation Overage (%)
West Kunlun	−6.3	50	32.3–34.0	2800–6700	0–30
Gaize	−0.3	200	34.5–36.1	4400–6000	0–80

4.2. Permafrost Characteristics and Vegetation in the Gaize

Vegetation types were regarded as possible indicators of the presence of permafrost at alpine regions [64]. Field works show that vegetation has great impact over the thermal condition and soil moisture content of the Gaize area [35]. Higher coverage for the same vegetation type tends to have lower soil temperature and higher soil moisture. In this study, remarkable impact of vegetation on the MAGT were found in the simulation over the borehole ZK 22 and borehole ZK 17, which are in the same gird cell and has adopted the same soil parameter and thermal roughness scheme. However, borehole ZK 17 was drilled on alpine meadow with 80% coverage, while borehole ZK 22 was drilled on alpine steppe with 40% coverage. Thus, the simulated MAGT of borehole ZK 17 was 2.0 °C lower than that of borehole ZK 22 due to their specific initial conditions and vegetation parameter

schemes. The results are consistent with the report by Li et al. [23] on the thermal state of permafrost, under different vegetation types, in the SADR of the eastern QTP.

Correlation between vegetation types and permafrost types of Gaize were further investigated by a revised Kappa analysis. Firstly, sub-stable permafrost, transitional permafrost, and unstable permafrost are integrated into pan-sub-stable permafrost type. Figure 11 shows the distribution of SFG, pan-sub-stable permafrost, and stable permafrost (Figure 11a) against distribution of BSV, alpine steppe, and alpine meadow (Figure 11b). Associating the pan-sub-stable permafrost with alpine steppe, SFG with BSV, and stable permafrost with alpine meadow, Kappa analysis can be conducted to check the correlation between the three permafrost types and vegetation types. Table 7 show that those permafrost types and vegetation types match each other well in the Gaize. SFG and BSV match best. Additionally, 82.4% of the cell grids adopting BSV as their vegetation parameter scheme were simulated as SFG, and 95.9% of the simulated SFG has BSV as their vegetation parameter scheme. Alpine steppe and pan-sub-stable permafrost ranks the second, and alpine meadow and stable permafrost ranks the last pair in match. Among the cell grids adopting alpine meadow as a vegetation parameter scheme, 69.9% were simulated as stable permafrost, and 57.6% of the simulated stable permafrost has alpine meadow as their vegetation parameter scheme, which means some stable permafrost occurs with other environmental constraints. Generally speaking, vegetation types in Gaize can substantially indicate the presence of certain permafrost. The Kappa coefficient for the distribution of permafrost types and vegetation types is 0.654, and the overall accuracy is 81.4%, which indicates that the two types substantially agree with each other.

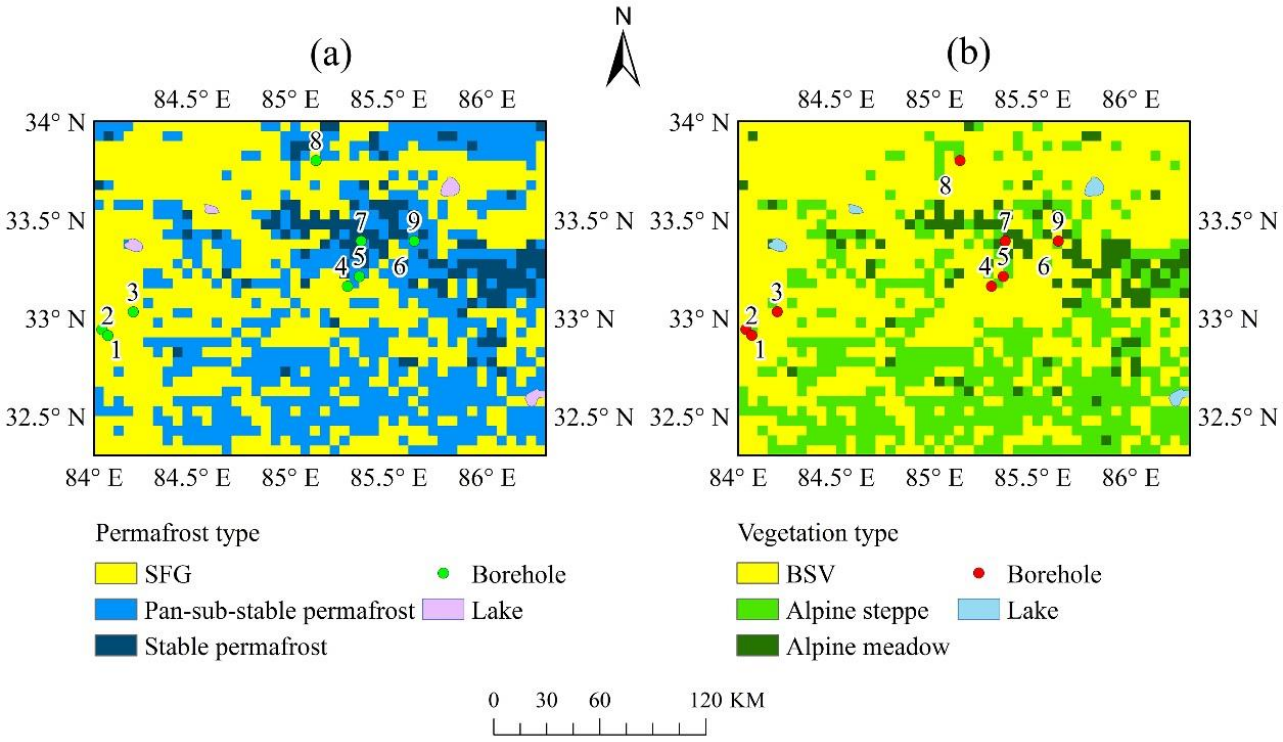

Figure 11. Distribution of (**a**) permafrost types and (**b**) vegetation types in the Gaize area (Borehole number 1 to 9 correspond to the borehole ID in Table 1).

Table 8 shows the MAGT range for different vegetation types in the Gaize. The average MAGT with different vegetation types in the Gaize can be listed in ascending order as alpine meadow < alpine steppe < BSV. The MAGT range of the three vegetation types overlap with each other, especially for the alpine meadow and alpine steep, indicating that the relationships between MAGT and vegetation types were rather complex. In the northeastern QTP, Li et al. [23] reported quite similar vegetation types to that of the Gaize,

such as Kobresia tibetica, Kobresia littledalei, and Kobresia pygmea, in the permafrost areas of SADR (98°30′–103°15′E, 36°30′–38°25′N). The vegetation distributed at a lower altitude with lower MAGT is compared with that of the Gaize.

Table 7. Environmental and meteorological factors at the West Kunlun and the Gaize area.

	Seasonally Frozen Ground	Pan-Sub-Stable Permafrost	Stable Permafrost	Total	** Accuracy of Permafrost Types Against Vegetation Types
BSV	814	173	1	988	82.4%
Alpine steppe	34	387	52	473	81.8%
Alpine meadow	1	30	72	103	69.9%
total	849	590	125	1564	
* accuracy of vegetation types against permafrost types	95.9%	65.6%	57.6%		
Overall accuracy	81.4%				
Kappa coefficeint	0.654				

* accuracy of vegetation types against permafrost types: the percentage of grid cells that have a certain type of vegetation and its corresponding permafrost type within the grid cells that have the type of permafrost—for example, the percentage of grid cells that have stable permafrost and alpine meadow within the grid cells that has stable permafrost. ** accuracy of permafrost types against vegetation types: the percentage of grid cells that have certain type of permafrost and its corresponding vegetation type within the grid cells that have the type of vegetation—for example, the percentage of grid cells that has stable permafrost and alpine meadow within the grid cells that has alpine meadow.

Table 8. The MAGTs and average MAGTs of soil layers with different vegetation cover in the Gaize area.

MAGT (°C)	BSV	Alpine Steppe	Alpine Meadow
Range of the MAGT (°C)	4.8~−2.0	3.8~−4.7	0.6~−4.8
Average MAGT (°C)	1.1	−1.7	−3.2

Stable permafrost occupies 8.0% of the total area of the Gaize. The MAGT of the stable permafrost in both the Gaize and the West Kunlun areas is about −3.6 °C. However, the average altitude of stable permafrost is 5364 m in the Gaize and 5768 m in the West Kunlun. The average altitude of the stable permafrost in the Gaize area is near to the average altitude of the transitional permafrost of the West Kunlun. Moreover, as the Gaize is located south of the West Kunlun, if the MAGT of any ground in the Gaize area is equal to that in the West Kunlun area, the altitude of the ground in Gaize ought to be higher according to the latitudinal zonality of ground temperature. The reversed average altitude of stable permafrost in the Gaize area indicates that alpine meadow has greatly influenced the altitudinal distribution of the stable permafrost in Gaize.

As growth of vegetation species in semi-arid areas such as Gaize is limited by soil moisture, they are more fragile to climate change than in the semi-humid SADR. Observation data from the meteorological station of the Gaize county show that MAAT and MAAP increase slowly during the year 2000 to 2010. It is believed that vegetation cover will decrease in response to permafrost thawing and drying soil caused by warming climate. However, increased precipitation could partially or fully offset drying soil, and the vegetation coverage of the Gaize area was found to increase slowly through MODIS NDVI analysis [55]. Therefore, the responses of alpine grassland to climate change and the corresponding permafrost changing are rather complicated. To project the permafrost degradation in transitional permafrost areas such as Gaize, reliable vegetation growth models allowing for the vegetation dynamics in the reginal scale during climate change is imperative.

5. Conclusions

Our study draws the following conclusions:

Using multi-source data, including remote sensing products, reliable databases, and field observations, permafrost characteristics and their relationship with local environmental constraints in the western QTP can be simulated by the augmented Noah with proper parametrization of the crucial environmental factors, such as soil and vegetation. Suitable simulation resolution can be scaled by MicroMet interpolation. The above methodology suggests that the modelling accuracy of permafrost characteristics of the transitional permafrost area, such as Gaize, can be gradually improved with parametrization schemes that match the local environmental conditions.

BSV, alpine steppe, and alpine meadow are the main vegetation types in the Gaize area. Modelling results show that those vegetation types are closely related to SFG, pan-substable permafrost, and stable permafrost, respectively. The occurrence of those vegetation types in Gaize can substantially indicate the presence of the corresponding permafrost. The altitudinal distribution of permafrost in the Gaize is greatly influenced by vegetation covers compared with that in the West Kunlun area, which is a predominantly stable permafrost distributed area. Permafrost distribution and characteristics in the Gaize are largely the composite consequence of altitude and vegetation.

Author Contributions: Conceptualization, H.C. and Z.N.; methodology, Y.W., H.C. and Z.N.; software and code, H.C. and Z.N.; formal analysis and investigation, Y.W., H.C. and Z.S.; resources, Z.N.; writing—original draft preparation, Y.W.; writing—review and editing, H.C. and Z.N.; funding acquisition, Z.N. All authors have read and agreed to the published version of the manuscript.

Funding: This research was funded by [the National Natural Science Foundation of China], grant NO. [41931180, 41971074], and [the Guangdong Provincial Department of Education], grant No. [GPDE [2020]20-374].

Data Availability Statement: Data are available upon request by email to the author.

Acknowledgments: The authors would like to thank the research group of "A synthesis dataset of permafrost for the Qinghai-Xizang (Tibet) Plateau, China (2002–2018)" for providing ground based datasets for model validation. The source code of augmented Noah LSM v3.4.1 was provided by the Permalab team of Nan Zhuotong (https://permalab.science/, accessed on 22 August 2021).

Conflicts of Interest: The authors declare no conflict of interest.

References

1. Wu, G.; Duan, A.; Liu, Y.; Mao, J.; Ren, R.; Bao, Q.; He, B.; Liu, B.; Hu, W. Tibetan plateau climate dynamics: Recent research progress and outlook. *Natl. Sci. Rev.* **2015**, *2*, 100–160. [CrossRef]
2. Yao, T.; Xue, Y.; Chen, D.; Chen, F.; Thompson, L.; Cui, P.; Koike, T.; Lau, K.M.; Lettenmaier, D.; Mosbrugger, V. Recent third pole's rapid warming accompanies cryospheric melt and water cycle intensification and interactions between monsoon and environment: Multidisciplinary approach with observations, modeling, and analysis. *Bull. Am. Meteorol. Soc.* **2019**, *100*, 423–444. [CrossRef]
3. Ran, Y.; Li, X.; Cheng, G.; Nan, Z.; Che, J.; Sheng, Y.; Wu, Q.; Jin, H.; Luo, D.; Tang, Z. Mapping the permafrost stability on the Tibetan plateau for 2005–2015. *Sci. China Earth Sci.* **2021**, *64*, 62–79. [CrossRef]
4. Eliseev, A.V.; Demchenko, P.F.; Arzhanov, M.M.; Mokhov, I.I. Transient hysteresis of near-surface permafrost response to external forcing. *Clim. Dyn.* **2014**, *42*, 1203–1215. [CrossRef]
5. Stendel, M.; Christensen, J.H. Impact of global warming on permafrost conditions in a coupled gcm. *Geophys. Res. Lett.* **2002**, *29*, 10-11–10-14. [CrossRef]
6. Riseborough, D.; Shiklomanov, N.; Etzelmüller, B.; Gruber, S.; Marchenko, S. Recent advances in permafrost modelling. *Permafr. Periglac. Process.* **2008**, *19*, 137–156. [CrossRef]
7. Cheng, G.D. Problems on zonation of high-altitude permafrost. *Acta Geograph. Sin.* **1984**, *39*, 185–193.
8. Smith, M.W.; Riseborough, D.W. Climate and the limits of permafrost: A zonal analysis. *Permafr. Periglac. Process.* **2002**, *13*, 1–15. [CrossRef]
9. Gądek, B.; Leszkiewicz, J. Influence of snow cover on ground surface temperature in the zone of sporadic permafrost, tatra mountains, poland and slovakia. *Cold Reg. Sci. Technol.* **2010**, *60*, 205–211. [CrossRef]
10. Yuan, L.; Rui, S.; Liu, S.M. Vegetation physiological parameter setting in the simple biosphere model 2(sib2) for alpine meadows in the upper reaches of Heihe River. *Sci. China Earth Sci.* **2015**, *58*, 755–769.

11. Baumann, F.; Schmidt, K.; Dörfer, C.; He, J.S.; Scholten, T.; Kühn, P. Pedogenesis, permafrost, substrate and topography: Plot and landscape scale interrelations of weathering processes on the central-eastern Tibetan plateau. *Geoderma* **2014**, *226*, 300–316. [CrossRef]
12. Rödder, T.; Kneisel, C. Influence of snow cover and grain size on the ground thermal regime in the discontinuous permafrost zone, Swiss Alps. *Geomorphology* **2012**, *175–176*, 176–189. [CrossRef]
13. Ishikawa, M.; Sharkhuu, N.; Zhang, Y.; Kadota, T.; Ohata, T. Ground thermal and moisture conditions at the southern boundary of discontinuous permafrost, mongolia. *Permafr. Periglac. Process.* **2005**, *16*, 209–216. [CrossRef]
14. Xiao, Y.; Zhao, L.; Dai, Y.J.; Li, R.; Pang, Q.Q. Representing permafrost properties in colm for the Qinghai-Xizang (Tibetan) plateau. *Cold Reg. Sci. Technol.* **2013**, *87*, 68–77. [CrossRef]
15. Gruber, S. Derivation and analysis of a high-resolution estimate of global permafrost zonation. *Cryosphere* **2012**, *6*, 221–233. [CrossRef]
16. Pang, Q.; Cheng, G.; Li, S.; Zhang, W. Active layer thickness calculation over the Qinghai-Tibet plateau. *Cold Reg. Sci. Technol.* **2009**, *57*, 23–28. [CrossRef]
17. Wu, Q.B.; Zhang, T.J.; Liu, Y.Z. Permafrost temperatures and thickness on the Qinghai-Tibet plateau. *Glob. Planet. Chang.* **2010**, *72*, 32–38. [CrossRef]
18. Wang, G.; Yuan, S.; Qing, B.; Wang, Y. Impacts of permafrost changes on alpine ecosystem in Qinghai-Tibet plateau. *Sci. China* **2006**, *49*, 1156–1169. [CrossRef]
19. Cao, B.; Zhang, T.; Wu, Q.; Sheng, Y.; Zou, D. Brief communication: Evaluation and inter-comparisons of Qinghai-Tibet plateau permafrost maps based on a new inventory of field evidence. *Cryosphere* **2019**, *13*, 511–519. [CrossRef]
20. Park, H.; Kim, Y.; Kimball, J.S. Widespread permafrost vulnerability and soil active layer increases over the high northern latitudes inferred from satellite remote sensing and process model assessments. *Remote Sens. Environ.* **2016**, *175*, 349–358. [CrossRef]
21. Zhao, L.; Hu, G.J.; Zou, D.F.; Wu, X.D.; Ma, L.; Sun, Z.; Yuan, L.M.; Zhou, H.Y.; Liu, S.B. Permafrost changes and its effects on hydrological processes on Qinghai-Tibet plateau. *Bull. Chin. Acad. Sci.* **2019**, *34*, 1233–1246.
22. Minsley, B.J.; Abraham, J.D.; Smith, B.D.; Cannia, J.C.; Voss, C.I.; Jorgenson, M.T.; Walvoord, M.A.; Wylie, B.K.; Anderson, L.; Ball, L.B. Airborne electromagnetic imaging of discontinuous permafrost. *Geophys. Res. Lett.* **2012**, *39*, L02503–L02510. [CrossRef]
23. Li, J.; Sheng, Y.; Chen, J.; Wu, J.; Wang, S. Variations in permafrost temperature and stability of alpine meadows in the source area of the datong river, northeastern Qinghai-Tibet plateau, China. *Permafr. Periglac.* **2014**, *25*, 307–319. [CrossRef]
24. Qin, Y.; Yi, S.; Chen, J.; Ren, S.; Ding, Y. Effects of gravel on soil and vegetation properties of alpine grassland on the Qinghai-Tibetan plateau. *Ecol. Eng.* **2015**, *74*, 351–355. [CrossRef]
25. Niu, F.; Gao, Z.; Lin, Z.; Luo, J.; Fan, X. Vegetation influence on the soil hydrological regime in permafrost regions of the Qinghai-Tibet plateau, China. *Geoderma* **2019**, *354*, 113892. [CrossRef]
26. Lin, Z.; Burn, C.R.; Niu, F.; Luo, J.; Liu, M.; Yin, G. The Thermal Regime, including a Reversed Thermal Offset, of Arid Permafrost Sites with Variations in Vegetation Cover Density, Wudaoliang Basin, Qinghai-Tibet Plateau. *Permafr. Periglac. Process.* **2015**, *26*, 142–159. [CrossRef]
27. Chen, R.; Yang, M.X.; Wang, X.J.; Wan, G.N. Review on simulation of land-surface processes on the Tibetan plateau. *Sci. Cold Arid. Reg.* **2019**, *11*, 93–115.
28. Wu, X.; Nan, Z.; Zhao, S.; Zhao, L.; Cheng, G. Spatial modeling of permafrost distribution and properties on the Qinghai-Tibet plateau. *Permafr. Periglac. Process.* **2018**, *29*, 86–99. [CrossRef]
29. Zhang, G.; Nan, Z.; Yin, Z.; Zhao, L. Isolating the contributions of seasonal climate warming to permafrost thermal responses over the Qinghai-Tibet plateau. *J. Geophys. Res. Atmos.* **2021**, *126*, e2021JD035218. [CrossRef]
30. Zhang, G.; Nan, Z.; Wu, X.; Ji, H.; Zhao, S. The role of winter warming in permafrost change over the Qinghai-Tibet plateau. *Geophys. Res. Lett.* **2019**, *46*, 11261–11269. [CrossRef]
31. Sun, S.; Zheng, D.; Liu, S.; Xu, Z.; Xu, T.; Zheng, H.; Yang, X. Assessment and improvement of noah-mp for simulating water and heat exchange over alpine grassland in growing season. *Sci. China Earth Sci.* **2022**, *65*, 536–552. [CrossRef]
32. Chang, Y.; Ding, Y.; Zhao, Q.; Qin, J.; Zhang, S. Optimization of canopy resistance models for alpine meadow in the northeastern Tibetan plateau. *J. Hydrol.* **2022**, *610*, 128007. [CrossRef]
33. Yang, K. High Spatial and Temporal Resolution Surface Meteorological Element Driven Dataset in China (1979–2015). National Cryosphere Desert Data Center. 2020. Available online: www.ncdc.ac.cn (accessed on 10 May 2020).
34. Liston, G.E.; Elder, K. A meteorological distribution system for high-resolution terrestrial modeling (micromet). *J. Hydrometeor.* **2006**, *7*, 217–234. [CrossRef]
35. Chen, J.; Zhao, L.; Sheng, Y.; Li, J.; Wu, X.; Du, E.; Liu, G.; Pang, Q. Some characteristics of permafrost and its distribution in the gaize area on the Qinghai-Tibet plateau, China. *Arct. Antarct. Alp. Res.* **2016**, *48*, 395–409. [CrossRef]
36. Wang, Z.; Wang, Q.; Zhao, L.; Wu, X.; Yue, G.; Zou, D.-F.; Nan, Z.; Liu, G.; Pang, Q.-Q.; Fang, H.-B.; et al. Mapping the vegetation distribution of the permafrost zone on the Qinghai-Tibet plateau. *J. Mt. Sci.-Engl.* **2016**, *13*, 1035–1046. [CrossRef]
37. Chen, H.; Nan, Z.; Zhao, L.; Ding, Y.; Chen, J.; Pang, Q. Noah modelling of the permafrost distribution and characteristics in the west kunlun area, Qinghai-Tibet plateau, China. *Permafr. Periglac. Process.* **2015**, *26*, 160–174. [CrossRef]
38. Zhao, L.; Zou, D.; Hu, G.; Wu, T.; Du, E.; Liu, G.; Xiao, Y.; Li, R.; Pang, Q.; Qiao, Y.; et al. A synthesis dataset of permafrost thermal state for the Qinghai-Tibet (Xizang) plateau, China. *Earth Syst. Sci. Data* **2021**, *13*, 4207–4218. [CrossRef]

39. Cheng, G.; Zhao, L.; Li, R.; Wu, X.; Sheng, Y.; Hu, G.; Zou, D.; Jin, H.; Li, X.; Wu, Q. Characteristic, changes and impacts of permafrost on Qinghai-Tibet plateau. *Chin. Sci. Bull.* **2019**, *64*, 2783–2795.
40. Zhao, L.; Zou, D.; Hu, G.; Du, E.; Pang, Q.; Xiao, Y.; Li, R.; Sheng, Y.; Wu, X.; Sun, Z.; et al. Changing climate and the permafrost environment on the Qinghai-Tibet (Xizang) plateau. *Permafr. Periglac. Process* **2020**, *31*, 396–405. [CrossRef]
41. Zhao, L.; Wu, T.; Xie, C.; Li, R.; Wu, X.; Yao, J.; Yue, G.; Xiao, Y. Support geoscience research, environmental management, and engineering construction with investigation and monitoring on permafrost in the Qinghai-Tibet plateau, China. *Bull. Chin. Acad. Sci.* **2017**, *32*, 1159–1168.
42. Guo, D.L.; Wang, H.J. Simulation of permafrost and seasonally frozen ground conditions on the Tibetan plateau, 1981–2010. *J. Geophys. Res.-Atmos.* **2013**, *118*, 5216–5230. [CrossRef]
43. Pan, X.; Li, X.; Yang, K.; He, J.; Zhang, Y.; Han, X. Comparison of downscaled precipitation data over a mountainous watershed: A case study in the heihe river basin. *J. Hydrometeor.* **2014**, *15*, 1560–1574. [CrossRef]
44. Zhang, L.; Ren, D.; Nan, Z.; Wang, W.; Wu, X. Interpolated or satellite-based precipitation? Implications for hydrological modeling in a meso-scale mountainous watershed on the Qinghai-Tibet plateau. *J. Hydrol.* **2020**, *583*, 124629. [CrossRef]
45. Zhao, Y.; Nan, Z.; Yu, W.; Zhang, L. Calibrating a hydrological model by stratifying frozen ground types and seasons in a cold alpine basin. *Water* **2019**, *11*, 985. [CrossRef]
46. Mernild, S.H.; Liston, G.E.; Hiemstra, C.; Wilson, R. The andes cordillera. Part iii: Glacier surface mass balance and contribution to sea level rise (1979–2014). *Int. J. Climatol.* **2017**, *37*, 3154–3174. [CrossRef]
47. Koch, S.E.; Desjardins, M.; Kocin, P.J. An interactive barnes objective map analysis scheme for use with satellite and conventional data. *J. Appl. Meteorol.* **1983**, *22*, 1487–1503. [CrossRef]
48. Liston, G.E.; Sturm, M. A snow-transport model for complex terrain. *J. Glaciol.* **1998**, *44*, 498–516. [CrossRef]
49. Iziomon, M.G.; Mayer, H.; Matzarakis, A. Downward atmospheric longwave irradiance under clear and cloudy skies: Measurement and parameterization. *J. Atmos. Sol. Terr. Phys.* **2003**, *65*, 1107–1116. [CrossRef]
50. Zheng, D.; Van der Velde, R.; Su, Z.; Wen, J.; Wang, X.; Booij, M.J.; Hoekstra, A.Y.; Lv, S.; Zhang, Y.; Ek, M.B. Impacts of noah model physics on catchment-scale runoff simulations. *J. Geophys. Res.: Atmos.* **2016**, *121*, 807–832. [CrossRef]
51. Shangguan, W.; Dai, Y.; Liu, B.; Zhu, A.; Duan, Q.; Wu, L.; Ji, D.; Ye, A.; Yuan, H.; Zhang, Q.; et al. A China data set of soil properties for land surface modeling. *J. Adv. Model. Earth Syst.* **2013**, *5*, 212–224. [CrossRef]
52. Gao, L.; Wang, X.; Johnson, B.A.; Tian, Q.; Wang, Y.; Verrelst, J.; Mu, X.; Gu, X. Remote sensing algorithms for estimation of fractional vegetation cover using pure vegetation index values: A review. *ISPRS J. Photogramm. Remote Sens.* **2020**, *159*, 364–377. [CrossRef]
53. Wang, X.; Yi, S.; Wu, Q.; Yang, K.; Ding, Y. The role of permafrost and soil water in distribution of alpine grassland and its ndvi dynamics on the Qinghai-Tibetan plateau. *Glob. Planet. Chang.* **2016**, *147*, 40–53. [CrossRef]
54. Kuang, W.; Dou, Y.; Zhang, C.; Chi, W.; Liu, A.; Liu, Y.; Zhang, R.; Liu, J. Quantifying the heat flux regulation of metropolitan land use/land cover components by coupling remote sensing modeling with in situ measurement. *J. Geophys. Res. Atmos.* **2015**, *120*, 113–130. [CrossRef]
55. Song, W.; Mu, X.; Ruan, G.; Gao, Z.; Li, L.; Yan, G. Estimating fractional vegetation cover and the vegetation index of bare soil and highly dense vegetation with a physically based method. *Int. J. Appl. Earth Obs. Geoinf.* **2017**, *58*, 168–176. [CrossRef]
56. Ge, J.; Meng, B.; Liang, T.; Feng, Q.; Gao, J.; Yang, S.; Huang, X.; Xie, H. Modeling alpine grassland cover based on modis data and support vector machine regression in the headwater region of the huanghe river, China. *Remote Sens. Environ.* **2018**, *218*, 162–173. [CrossRef]
57. Chen, Y.Y.; Yang, K.; Zhou, D.G.; Qin, J.; Guo, X.F. Improving the noah land surface model in arid regions with an appropriate parameterization of the thermal roughness length. *J. Hydrometeor.* **2010**, *11*, 995–1006. [CrossRef]
58. Zilitinkevich, S.S. *Non-Local Turbulent Transport: Pollution Dispersion Aspects of Coherent Structure of Convective Flows, Air Pollution Theory and Simulation*; Power, H., Moussiopoulos, N., Brebbia, C., Eds.; Computational Mechanics Publications: Boston, MA, USA, 1995; pp. 53–60.
59. Wang, Z.W.; Wu, X.D.; Yue, G.Y.; Zhao, L.; Wang, Q.; Nan, Z.-T.; Qin, Y.; Wu, T.-H.; Shi, J.-Z.; Zou, D.-F. Spatial and temporal variations in spectrum-derived vegetation growth trend on the Qinghai-Tibetan plateau from 1982 to 2014. *Spectrosc. Spectr. Anal.* **2016**, *36*, 471–477.
60. Kumar, A.; Chen, F.; Niyogi, D.; Alfieri, J.G.; Ek, M.; Mitchell, K. Evaluation of a photosynthesis-based canopy resistance formulation in the noah land-surface model. *Bound.-Lay. Meteorol.* **2010**, *138*, 263–284. [CrossRef]
61. Zou, D.; Zhao, L.; Sheng, Y.; Cheng, G. A new map of permafrost distribution on the Tibetan plateau. *Cryosphere* **2017**, *11*, 2527–2542. [CrossRef]
62. Wang, T.; Yang, D.; Fang, B.; Yang, W.; Qin, Y.; Wang, Y. Data-driven mapping of the spatial distribution and potential changes of frozen ground over the Tibetan plateau. *Sci. Total Environ.* **2019**, *649*, 515–525. [CrossRef]
63. Liu, Y.; Wu, X.; Wu, T.; Zhao, L.; Li, R.; Li, W.; Hu, G.; Zou, D.; Ni, J.; Du, Y. Soil texture and its relationship with environmental factors on the Qinghai-Tibet plateau. *Remote Sens.* **2022**, *14*, 3797. [CrossRef]
64. Shi, Y.; Niu, F.; Yang, C.; Che, T.; Lin, Z.; Luo, J. Permafrost presence/absence mapping of the Qinghai-Tibet plateau based on multi-source remote sensing data. *Remote Sens.* **2018**, *10*, 309. [CrossRef]